



# Wet bias of summer precipitation in the northwestern Tibetan Plateau in ERA5 is linked to overestimated lower-level southerly wind over the plateau

Tinghai Ou<sup>1</sup> · Deliang Chen<sup>1</sup> · Jianping Tang<sup>2,3</sup> · Changgui Lin<sup>1</sup> · Xuejia Wang<sup>4</sup> · Julia Kukulies<sup>1</sup> · Hui-Wen Lai<sup>1</sup>

Received: 15 June 2022 / Accepted: 5 January 2023 / Published online: 16 January 2023  
© The Author(s) 2023

## Abstract

The Tibetan Plateau (TP), also called the Third Pole, is considered to be “the world water tower”. The northwestern TP (NWTP), which has an average elevation higher than 4800 m, is an arid region where the summer precipitation is largely overestimated by the ERA5 global reanalysis product. We hypothesize that this wet bias is mainly caused by unrealistic lower-level winds that trigger strong convection over the region; it can be reduced by using a high-resolution regional climate model with a large domain that allows realistically representing interactions between the Westerlies and Asian summer monsoons. Here, downscaling using the Weather Research and Forecasting (WRF) model driven by ERA5 was conducted with a large domain (8°–50° N, 65°–125° E) at 9 km for the period 1979–2019 (WRF9km). Precipitation values from WRF9km and ERA5 were evaluated against satellite observations; compared with ERA5, WRF9km captured the climatological summer precipitation over the NWTP with a much-reduced wet bias. The ERA5 overestimation is mainly caused by excessive convective precipitation, likely linked to strong vertical motions over the NWTP induced by an overestimated lower-level southerly wind.

**Keywords** Tibetan Plateau · Summer precipitation · ERA5 · WRF · Wind

## 1 Introduction

The Tibetan Plateau (TP), also called the Third Pole, is the most extensive area of high land in the world. Many of the major rivers of Asia (e.g., Yangtze, Yellow, Mekong, Brahmaputra, Indus, Ganges, Amu Darya, and Syr Darya) originate from the TP, providing water for billions of people downstream. The TP is also considered to be “the world water tower” (Xu et al. 2008) and is often referred to as “the

roof of the world”. The TP, as a typical alpine zone with apparent ecosystem vulnerability and sensitivity, holds fundamental ecological and environmental significance to China and Asia (Latif et al. 2019). Under the background of global warming, temporal and spatial characteristics of precipitation have undergone dramatic changes across the TP (Xiong et al. 2019), with ecosystems under increasing pressure (Li and Song 2021). Increasing temperature and redistributed precipitation extensively affect ecosystem productivity on the plateau by affecting the biological, hydrological, and ecological processes (Guo et al. 2016; Shen et al. 2022; Wan et al. 2017). Typically, the ecosystem vulnerability in the northwest was greater than that in the southeast. Thus, an investigation into precipitation variability, patterns, and related physical processes in this region is meaningful for ecosystem function and land management (Weltzin et al. 2003). The northwestern TP (NWTP, 33°–36° N, 80°–90° E), which has an average elevation higher than 4800 m, is an arid region, a large part of which has an annual precipitation of less than 250 mm (Wang et al. 2018). A large part of the largest National Nature Reserve in China, the Qiangtang National Nature Reserve, is also located on the NWTP (Li

✉ Deliang Chen  
deliang@gvc.gu.se

<sup>1</sup> Regional Climate Group, Department of Earth Sciences, University of Gothenburg, 40530 Gothenburg, Sweden

<sup>2</sup> Key Laboratory of Mesoscale Severe Weather/Ministry of Education, Nanjing University, Nanjing, China

<sup>3</sup> School of Atmospheric Sciences, Nanjing University, Nanjing, China

<sup>4</sup> Key Laboratory of Western China’s Environmental Systems (Ministry of Education), College of Earth and Environmental Sciences, Lanzhou University, Lanzhou, China

and Pimm 2020). The NWTP possesses a largely intact ecosystem including permafrost, alpine vegetation, lakes, and wild animals, with little disturbance from human activities. The ecosystem is markedly affected by climate because the available precipitation is limited. In addition, the NWTP has recently experienced an increase in summer precipitation and expansion of lakes (Sun et al. 2020), while the glacier contraction rate is smaller than in other regions in China (Su et al. 2022; Yao et al. 2012). Permafrost has been indicated to degrade in the area because of increasing temperatures (Yang et al. 2019), and alpine vegetation is ecologically vulnerable to climate change due to its spatial distribution and rapid warming in high elevation (Wang et al. 2017; You et al. 2020). Hence, this region can act as a test bed to study land–atmosphere interactions and has vital implications for the study of climate change.

The northern TP is climatically controlled by westerlies and the southern TP is mainly influenced by Indian monsoon circulation (Chen et al. 2009), which is critical for advection and moisture transport. According to Yao et al. (2013), due to the effect of the elevated topography of TP, the westerly winds bifurcate into two branches over the Caspian Sea: one passes by the northern side of the plateau and the other flows around the southern side of the plateau. These two branches then meet to the east of the plateau (Liu and Yin 2001), with an anticyclone to the north of the TP and a cyclone to the south. Although the westerlies reaching the TP are characterized by low moisture, the Indian summer monsoon brings substantial precipitation to this generally semi-arid region (Zhu et al. 2015). The westerlies anomaly associated with the North Atlantic Oscillation may be primarily responsible for shaping the pattern of the north–south precipitation gradient (Liu and Yin 2001). In addition to the precipitation climatology, precipitation trends also show a clear regional heterogeneity, increasing in the north and decreasing in the south, with more detailed studies finding positive anomalies over most of the central and eastern Himalaya and negative anomalies over the Karakoram, western Himalaya, and far eastern Himalaya (Krishnan et al. 2019). This heterogeneity is attributed to the dominance of the weakened Indian monsoon over the south and the significantly strengthened westerlies (e.g., An et al. 2012; Forsythe et al. 2017). In turn, the elevated topography of the TP not only acts as a barrier to the midlatitude westerlies but also affects the Indian monsoon through its dynamic and thermal impacts, with dominant thermal forcing in spring and summer, and mechanical forcing in winter (Wu et al. 2015), thus contributing to large-scale atmospheric circulation (Bothe et al. 2011).

Summer precipitation over the NWTP is markedly influenced by both the Westerlies and Asian summer monsoons (e.g., Feng and Zhou 2012; Schiemann et al. 2009; Ye 1981; Zhang et al. 2019a, b). In the summer season, the core of the East Asia Westerly Jet (EAWJ) moves northwards to

the northern edge of the TP at approximately 40° N (Schiemann et al. 2009; Yu et al. 2021); this is associated with northward water vapor transport to the NWTP (Feng and Zhou 2012). At the same time, the upper-tropospheric subtropical Westerlies are located around 40° N over the TP, where the EAWJ is also present (Schiemann et al. 2009). As a result, a large proportion of the precipitation falls over a region that is jointly affected by the Westerlies and Indian summer monsoon (Lai et al. 2021). Most of the TP vortices (mesoscale weather systems active in the near-surface of the TP) are generated over the NWTP (Curio et al. 2019; Lin et al. 2020), which has a large impact on precipitation over the whole TP and even downstream East Asia. On the other hand, the high mountains may act as an obstacle to the flow of the Westerlies, and the induced orographic forcing may thereby have a great impact on the northerly wind branches of the summer Westerlies across the TP (Kong and Chiang 2020; Molnar et al. 2010).

An accurate representation of the interaction between the Westerlies and the high mountains is critical to enable the realistic simulation of local circulation and precipitation over the NWTP. Precipitation over the NWTP, especially in the summer season, is generally overestimated by global reanalysis products, global climate models, and regional climate models (RCMs) with a horizontal resolution coarser than 20 km (e.g., Gao et al. 2020b; Li et al. 2015; Liang et al. 2021; Sun et al. 2021; Tong et al. 2014; Wang et al. 2021). The overestimated summer precipitation over the NWTP may be reduced by RCMs by increasing the horizontal resolution, especially by convection-permitting models (CPMs; with grid spacings no coarser than 5 km) (Gu et al. 2020; Li et al. 2021; Lin et al. 2018). However, this was not shown to be the case in the work of Ma et al. (2021a), in which an overestimated summer precipitation over the NWTP persisted in their CPM simulations with a horizontal resolution of 3 km. The overestimated precipitation is not simply a scale-dependent problem related to the impacts of small-scale features, and therefore the overestimation may not be reduced by simply increasing the horizontal resolution. Important dynamics, such as the interaction between the Westerlies and the high plateau, should also be addressed to better understand the mechanisms behind the overestimated precipitation.

Following approximately thirty years of development, RCMs are now widely used to study small-scale processes and climate change simulations (Giorgi 2019). However, RCMs are sensitive to different model configurations, such as domain size and horizontal resolution (Giorgi 2019). The wet bias over the NWTP is reduced in the High Asia Refined analysis version 2 (HARv2) at 10 km horizontal resolution, compared with its previous version (HAR), even if there is a general increase in the precipitation over a large part of the TP (Wang et al. 2020). One of the main changes in

HARv2 compared with HAR is that the domain of the 10 km simulation has been extended northwards to the north of 45° N, and now covers the location of the core of the summer upper-tropospheric subtropical Westerlies. We observed that the northern boundaries of the RCMs used in the work of Ou et al. (2020) and Ma et al. (2021a) were at approximately 40° N, which may affect the ability of their models to capture the interactions between the Westerlies, Asian summer monsoons, and high plateau. A recent study by Prein et al. (2022), based on a set of cross-model CPM case study simulations, also indicated that the domain boundaries of RCMs are very important in enabling the realistic simulation of precipitation over the TP; their simulations with larger domains performed better than those with relatively smaller domains, with the northern boundary located at approximately 40° N. Therefore, we here propose a large domain RCM simulation, with the northern boundary covering the location of the core of the summer upper-tropospheric subtropical Westerlies over the TP; we use this to examine the ability of a RCM to simulate summer precipitation over the NWTP. We hypothesize that a RCM with such a large domain, which may develop its own climatology and potentially modify some large-scale climate structures more realistically, can successfully capture the interactions between the Westerlies, Asian summer monsoons, and high plateau, and in turn, realistically simulate the precipitation climatology over the NWTP.

To test and confirm this hypothesis, the fifth-generation global reanalysis product from the European Centre for Medium-Range Weather Forecasts (ECMWF), ERA5 (Hersbach et al. 2020), was utilized to drive Weather Research and Forecasting (WRF) simulations. The remainder of this manuscript is organized as follows: Sect. 2 introduces the data, model configuration, and methods; the results of precipitation evaluation and analysis of related circulations are presented in Sect. 3; and in Sect. 4, we give the discussion and conclusions.

## 2 Data, model configuration, and methods

### 2.1 Data sets

To compare the representation of summer precipitation over the NWTP, hourly precipitation products from ERA5 and HARv2, a 10 km dynamic downscaling driven by the ERA5, were used. Re-initialization scheme (daily initialization which will run for 36 h with the first 12 h as spin-up time) was adopted in HARv2 similar to its previous version, HAR. Initial snow depth was corrected based on Japanese 55-year Reanalysis (JRA-55) in HARv2, which has shown to have a better representation of air temperature at 2 m but with slightly higher precipitation amounts than HAR (Wang

et al. 2020). The ERA5 data is available at hourly intervals from 1979 to the present with a horizontal resolution of  $0.25^\circ \times 0.25^\circ$ , while HARv2 is currently available at hourly intervals during the period 1991–2019.

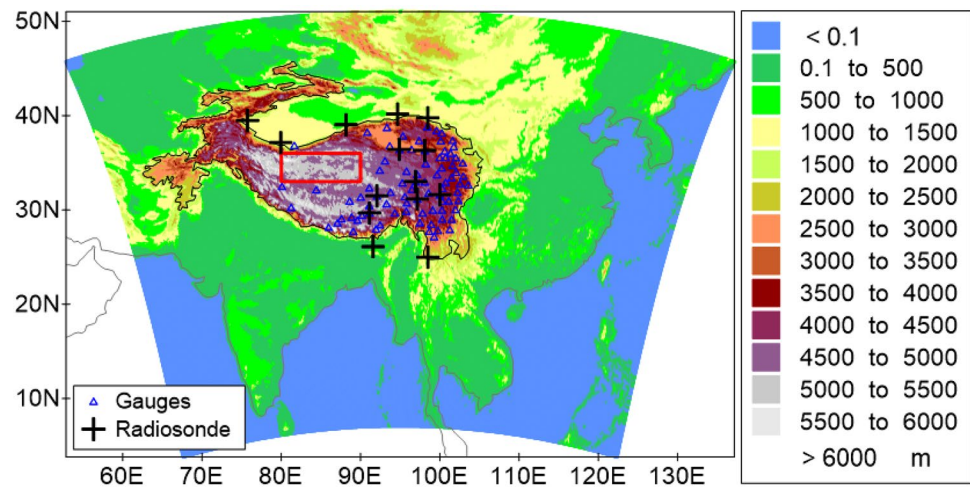
The study region is mainly located in the permafrost region of the TP (Zou et al. 2017). Owing to the harsh environment across the NWTP, only a few in situ observations are available (Wang et al. 2018); these are insufficient to study the climatic characteristics of precipitation. The Integrated Multi-satellitE Retrievals for GPM (IMERG) precipitation product version 06, available at half-hourly intervals from June 2000 to the present, was used as a reference data set for precipitation (Huffman et al. 2019a, b). It fuses precipitation estimates from the TRMM satellite (2000–2015) with more recent precipitation estimates from the GPM satellite (2014–present). The IMERG precipitation product has a horizontal resolution of  $0.1^\circ \times 0.1^\circ$  and shows good performance in the capturing of diurnal cycles and seasonal and inter-annual variations of in situ observed precipitation across China (Ma et al. 2021b; Tang et al. 2020). The half-hourly IMERG values were summed to get hourly precipitation. To have a better view of the reliability of satellite products, both the calibrated (IMERG) and uncalibrated (IMERG\_Uncal) precipitation products by gauge observations from IMERG were utilized.

Daily gauge observations from 83 stations during 1980–2016, following the study of Gao et al. (2015), were also used to evaluate the reliability of IMERG precipitation in capturing the observed mean and seasonal cycles over the whole TP, providing indirect support for the robustness of using IMERG precipitation as a reference over the NWTP (Fig. 1).

Pressure-level zonal ( $u$ ), meridional ( $v$ ), and vertical wind ( $w$ ) from ERA5 were adopted to examine changes in pressure-level circulation, especially lower-level wind (i.e., 500 hPa). The monthly mean of observed  $v$ -wind at 00:00 and 12:00 UTC at 14 radiosonde stations from the Integrated Global Radiosonde Archive (IGRA) was used to evaluate the lower-level wind (Durre et al. 2006, 2018) (Fig. 1). These stations all have records lasting more than 10 years over the period 1980–2019.

Cloud cover fraction (CCF) was the portion of grids that were covered by clouds ranging from 0% to 100%. A 100% of CCF meant a totally cloudy day, while a 0% of CCF indicated a clear day with no visible clouds at all. Three-dimensional CCF can be used to illustrate the horizontal and vertical distribution of the cloud cover. In the present work, pressure-level CCF from ERA5 and the observational CloudSat product 2B-GEOPROF-LIDAR were used to evaluate the simulated cloud cover over the TP. 2B-GEOPROF-LIDAR is a combined product of the spaceborne lidar sensor Cloud-Aerosol Lidar with Orthogonal Polarization (CALIOP) and the radar sensor Cloud Profiling Radar (CPR)

**Fig. 1** WRF model domain with topography (black line encloses the main body of the Tibetan Plateau with an elevation above 2000 m; red rectangle shows the location of the northwestern Tibetan Plateau [33°–36°N, 80°–90°E]; black crosses show the location of radiosonde stations; blue triangles show the location of the 83 gauges)



(Mace and Zhang 2014; Marchand et al. 2008). Following Kukulies et al. (2019), we used radar–lidar combined cloud fractions to ensure that both clouds with thicker optical depths and clouds with large contents of ice particles were accounted for. The 2B-GEOPROF-LIDAR CCF is available from 2006 to 2010. Elevation over the TP was illustrated using the 90 m topographic data from the Shuttle Radar Topography Mission (SRTM) (Reuter et al. 2007).

## 2.2 WRF model configuration

Herein, the WRF model version 3.7.1 in the non-hydrostatic configuration (Skamarock et al. 2008) was used to dynamically downscale global reanalysis data with the domain centered over the TP. The model domain was configured at 9 km grid spacing and centered at 29.0° N, 95.0° E, with 730 grid points in the east–west direction and 550 grid points in the north–south direction (Fig. 1). There were 60 eta levels, with the model top at 10 hPa. The northernmost boundary of the domain was extended to approximately 50° N, which covers the core of the summer upper-tropospheric subtropical Westerlies. Specifically, the New Goddard short-wave radiation (Chou and Suarez 1999), RRTMG long-wave radiation (Iacono et al. 2008), WRF Double Moment 6-class (Lim and Hong 2010), Unified Noah Land Surface Model (Tewari et al. 2004), Revised MM5 surface layer (Jiménez et al. 2012), and Yonsei University (YSU) Planetary Boundary Layer (PBL) (Hong et al. 2006) schemes were used in the WRF experiments. Similar to previous work by Ou et al. (2020), cumulus parameterization was turned off because, by doing this, the model can successfully capture the precipitation climatology over the plateau at gray-zone grid spacing.

Spectral nudging (Kida et al. 1991), which can be regarded as an indirect data assimilation method (von Storch et al. 2000), was used in this work. Previous studies

have shown that dynamic downscaling of global reanalysis products with spectral nudging can successfully capture the precipitation climatology over the TP (Ma et al. 2021a; Ou et al. 2020). Following the approach of spectral nudging adopted by Ou et al. (2020) and Liu et al. (2017), nudging was applied to atmospheric levels above the approximate PBL top, increasing the magnitude linearly to the full amount at the fifth level above the PBL. A common nudging coefficient ( $0.0003 \text{ s}^{-1}$ ) was used for all variables (geopotential, horizontal wind, and temperature) to adjust the strength of the nudging force in the governing equations. The wavenumber truncations were set to 6 and 4, corresponding to cut-off wavelengths of approximately 1095 and 1238 km in the zonal and meridional directions, respectively; this is close to the value of 1000 km suggested by Gómez and Miguez-Macho (2017) and Mai et al. (2020).

The initial and boundary conditions, including sea surface temperature (SST), were provided by ERA5, in which the boundary information (including SST) is updated every 3 h. To save the time spent on long-term simulations, two parallel continuous simulations (1979–1998 and 1998–2019) were conducted simultaneously. The differences in regional average precipitation, relative humidity (RH), near-surface air temperature (T2m), surface skin temperature (Tsfc), and surface net radiation were relatively small between the two parallel continuous simulations at the end of the overlapping year (1998) (Fig. S1). Therefore, the one-year overlap strategy introduced little disturbance into the simulations, and we were able to combine the two simulations (1979–1998 and 1999–2019) into one continuous simulation covering the period 1979–2019. Hereafter, this simulation is referred to as WRF9km, with the first year (1979) treated as a spin-up period and discarded from analysis.

## 2.3 Methods

In the current work, in-situ observations, regular grid data products from ERA5 and IMERG, and simulations with equal distance grids from WRF9km and HARv2 were used. To compare precipitation from different products with in-situ observations, precipitation of the grid in which a gauge was located was selected. Hourly precipitation from ERA5, HARv2, IMERG, and WRF9km from 08 to 08 AM of the next day were further summed to get daily precipitation with the same time interval of in-situ observation. Total precipitation (including both liquid and solid precipitation) were used in the current work for ERA5, WRF9km, HARv2, and IMERG. For WRF9km, only accumulated total grid-scale precipitation (non-convective) was involved since cumulus schemes were turned off. All the products (ERA5, HARv2, IMERG, and WRF9km) were interpolated to  $0.1^\circ \times 0.1^\circ$  regular grid using the Kriging method for spatial comparison.

There were no direct snowfall products in IMERG. However, IMERG products contained the probability of liquid precipitation, which can be used to detect snowfall (Li et al. 2022). Following the study of Li et al. (2022), the hourly precipitation (calibrated IMERG precipitation) can be classified as snowfall if the probability of liquid precipitation is  $<20\%$  over the TP during the observation hour. The hourly precipitation that was classified as snowfall was summed to get the daily and monthly snowfall amounts.

## 3 Results

### 3.1 Evaluation of simulated precipitation in different data sets over the whole TP

Gauge observations from 83 stations were used to evaluate the seasonal cycle and interannual variation in both simulated and IMERG precipitation over the TP. The observed seasonal cycle of precipitation averaged over the TP was accurately captured by WRF9km, while ERA5 and HARv2 showed overestimated mean precipitation throughout the year (Fig. 2a). Compared with the work of Gao et al. (2015), who used WRF with a horizontal resolution of 30 km, WRF9km demonstrated the advantage of high-resolution simulations, producing a reduced wet bias. On average, there was a slight dry bias in the summer season and a slight wet bias in the winter season in WRF9km; the dry bias in the summer season was mainly located over the center of the southern TP (north of the Himalayas; Fig. 3), while the wet bias in the winter season was found over the whole southern TP (figure not shown). Further investigation is required to discover the causal factors of these biases. The wet bias in the winter season was stronger when averaged over the whole TP (higher than 2000 m) which could be related to strong snowfall as can be inferred from the summer snowfall contribution (Fig. 4). ERA5 and the two downscaling products of ERA5 (WRF9km and HARv2) had a large contribution of snowfall to the total summer precipitation, especially over the northwest TP (Fig. S2). While snowfall calculated from the IMERG product had a lower amount and

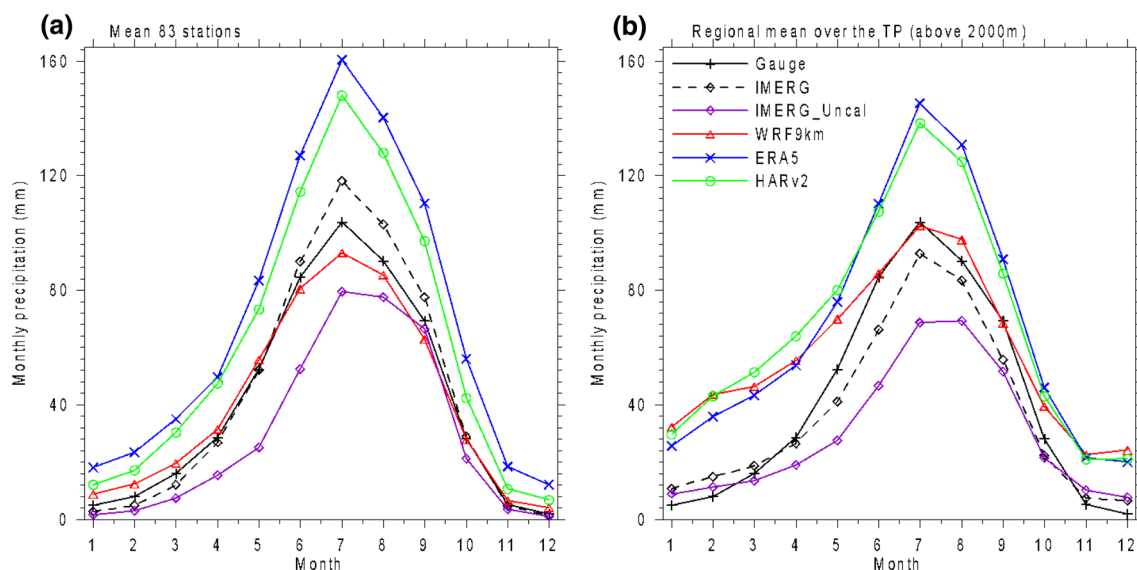


**Fig. 2** Seasonal variation in precipitation (mm) averaged over the TP obtained from 83 gauges, **a** compared with the gauge-adjacent grids of IMERG (IMERG: precipitation—calibrated; IMERG\_Uncal: pre-

cipitation—uncalibrated), ERA5, HARv2, and WRF9km, and **b** compared with the mean over the region [66.5–105.5°E, 24.5–41.0°N] with an elevation higher than 2000 m during the period 2001–2016

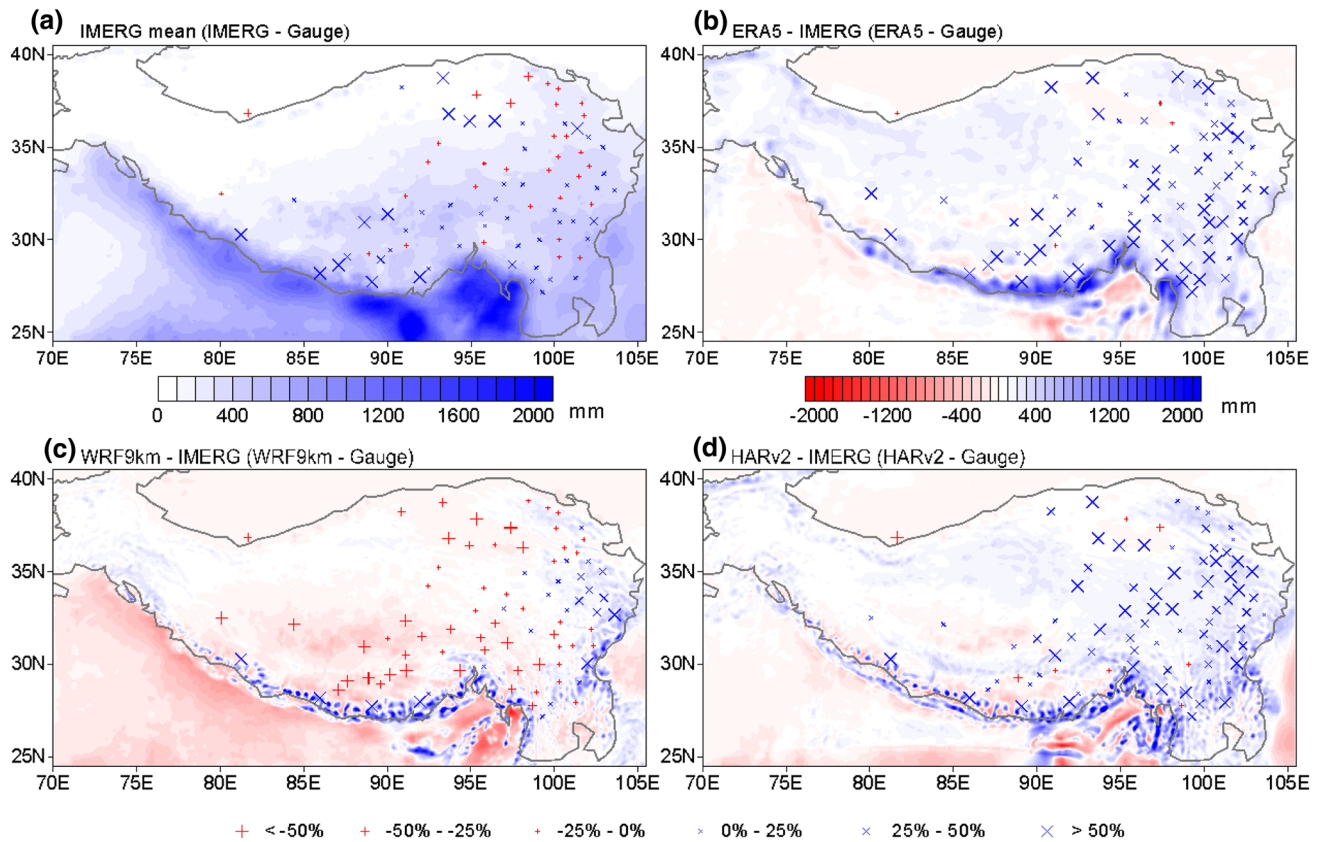


**Fig. 3** Summer mean total precipitation (mm) during the period 2000–2019 from IMERG (a) and the differences of summer mean total precipitation (mm) between three products (ERA5, WRF9km,

and HARv2) and IMERG (shading) (b–d) and the percentage differences (%) between four products (IMERG, ERA5, WRF9km, and HARv2) and gauge observations (crosses; a–d)

contribution to summer total precipitation compared with ERA5, WRF9km, and HARv2. Casella et al. (2017) also reported that the GPM carried spaceborne Dual-frequency Precipitation Radar (DPR) only detected around 5–7% of the snowfall events and 27–34% of the snowfall mass over the United States. Microphysics schemes that may affect the snowfall simulations (e.g. Gao et al. 2020a) need further evaluation.

The IMERG precipitation captured the seasonal cycle of the gauge observations quite well, but with a slight overestimation of precipitation in the summer season and a slight underestimation in the winter season (Fig. 2). Compared to IMERG, IMERG\_Uncal underestimated the precipitation over the TP throughout the year. This can be seen from both the average of the 83 stations and the mean of the high mountain region with an elevation higher than 2000 m. This indicated that the station calibration procedure has significantly increased the climate mean of total precipitation in IMERG. The influence of the calibration on the climate mean of total precipitation was not only over the station grids but also the whole TP. Generally, IMERG precipitation overestimated summer total precipitation compared to

that of the in-situ observations (Fig. 3a). The overestimation tended to be larger than 25% over western TP. However, several factors, such as wind-induced error, wetting loss, evaporation loss, and trace amount, may cause undercatch of precipitation over the TP (e.g. Ma et al. 2015; Zhang et al. 2019a, b). Ma et al. (2015) reported the total effects of these factors on the annual total precipitation can lead to an undercatch of an average of 27% over the TP. Zhang et al. (2019a, b) also reported that the percentage of undercatch is largest during the winter season and least during the summer season. The total undercatch during the summer season is less than 20% over the eastern TP (Zhang et al. 2019a, b). Besides, undercatch of snow by the gauges may also increase uncertainties of station observation (e.g. Fasnacht 2004; Yang et al. 2000). Overall, IMERG precipitation products can be regarded as a good alternative to gauge observations over the TP where there were limited observations available.

Spatially, both ERA5 and HARv2 overestimated summer precipitation by 25% over most parts of the TP compared with gauge observations, with an overestimation of more than 50% over southern TP in ERA5 and the center of eastern TP in HARv2 (Fig. 3b, d). WRF9km underestimated

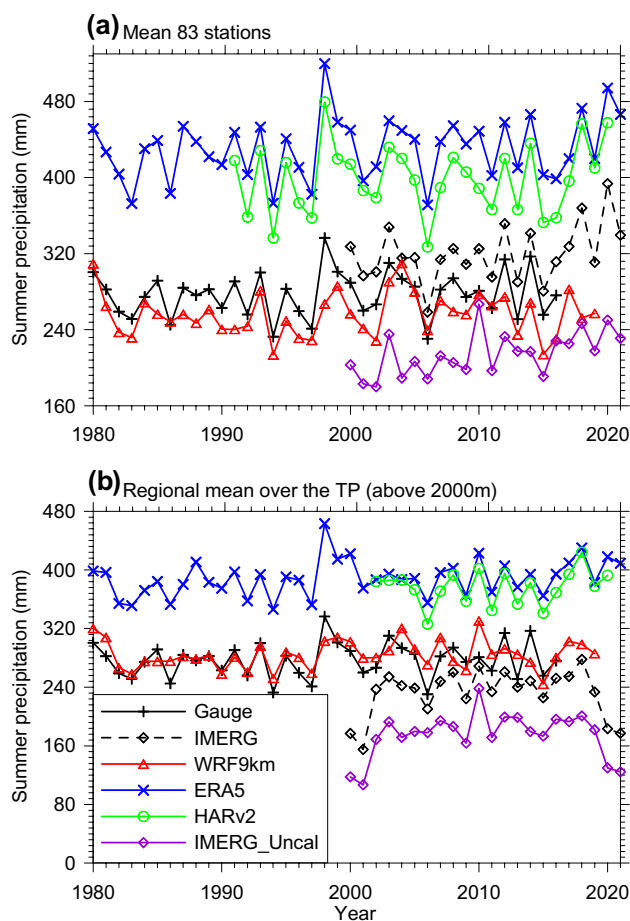


**Fig. 4** **a** Time series of the interannual variation in summer (June–July–August) total precipitation (mm) over the TP obtained from 83 gauges, as well as the precipitation from gauge-adjacent grids of IMERG, IMERG\_Uncal, ERA5, HARv2, and WRF9km during the period 1980–2021. **(b)** Same as **(a)** but the time series from IMERG, IMERG\_Uncal, ERA5, HARv2, and WRF9km are the mean over the region [66.5–105.5°E, 24.5–41.0°N] with an elevation higher than 2000 m

summer precipitation by 25–50% over western TP while overestimated by about 25% over eastern TP (Fig. 3b). By considering the undercatch of gauge observations, the ERA5 and HARv2 had a general overestimation of precipitation over the TP, while WRF9km had a reasonably captured precipitation over the eastern TP and a dry bias over the south-of-center TP. Compared with IMERG, a dry belt can also be found over the south-of-center TP in both ERA5 and HARv2. Interesting to mention that there were clear effects of meridional canyons on summer precipitation over the Himalaya mountain range in the downscaled products (WRF9km and HARv2), with even stronger precipitation in WRF9km than HARv2.

We further evaluated the interannual variation of summer precipitation averaged over the whole TP (Fig. 4). Both ERA5 and HARv2 consistently overestimated (by

54% and 40%, respectively, when averaged over the period 2000–2016) summer precipitation compared with the mean of 83 gauge observations. In contrast, WRF9km successfully captured the observed interannual variation of summer mean precipitation over the TP, but with a slight dry bias (−7%). The same conclusion can be drawn when comparing the summer mean precipitation averaged over all the grids with an elevation higher than 2000 m (Fig. 4b). The annual variation of IMERG precipitation agreed quite well with gauge observations, but with a slight overestimation for summer (12%). IMERG\_Uncal, again, showed an underestimated summer precipitation compared with both gauge observations and IMERG.

To further evaluate the simulated precipitation, the probability density function (PDF) of both daily and hourly precipitation was assessed (Fig. 5). On the daily scale, IMERG agreed with gauge observation quite well, albeit with a high probability of heavy precipitation. Given the undercatch of precipitation by gauge observations, IMERG product can well illustrate the PDF of summer precipitation over the TP. ERA5 overestimated light to moderate precipitation compared to both gauge and satellite precipitation, with the lowest frequency of days with daily precipitation < 1 mm (especially for daily precipitation < 0.1 mm) than the other data sets assessed. This may be due to the “drizzle problem” in climate models induced by cumulus schemes (e.g. Chen and Dai 2019). Interesting to mention that the probability of heavy precipitation (daily precipitation between 20–50 mm) in ERA5 was close to gauges. HARv2 presented a generally overestimated frequency of days with daily precipitation higher than 0.1 mm compared to both gauge and satellite precipitation. WRF9km had the highest frequency of days with daily precipitation < 0.1 mm compared to the other data sets. On average, the frequency of daily precipitation < 15 mm is underestimated by WRF9km, while its frequency of days with daily precipitation larger than 15 mm is similar to that of IMERG (higher than gauge observations).

On the hourly scale, 85% of hours had precipitation < 0.1 mm in IMERG, while it was 64%, 92%, and 80% for ERA5, WRF9km, and HARv2 separately. WRF9km had a low frequency of hours with hourly precipitation between 0.1 and 3.0 mm than IMERG, while WRF9km had a higher frequency of hours with hourly precipitation larger than 3 mm compared with IMERG. This may be due to the cumulus scheme being turned off in WRF9km. Ou et al. (2020) reported that there was a low frequency of hours with hourly precipitation smaller than 2.0 mm in the simulations with cumulus schemes being turned off than the ones with a cumulus scheme at the grid space of 9 km. Compared with IMERG, HARv2 had a higher frequency of hours with hourly precipitation less than 4.0 mm, while a lower frequency of hours with hourly precipitation larger than 4.0 mm. ERA5 was similar to HARv2 but with a

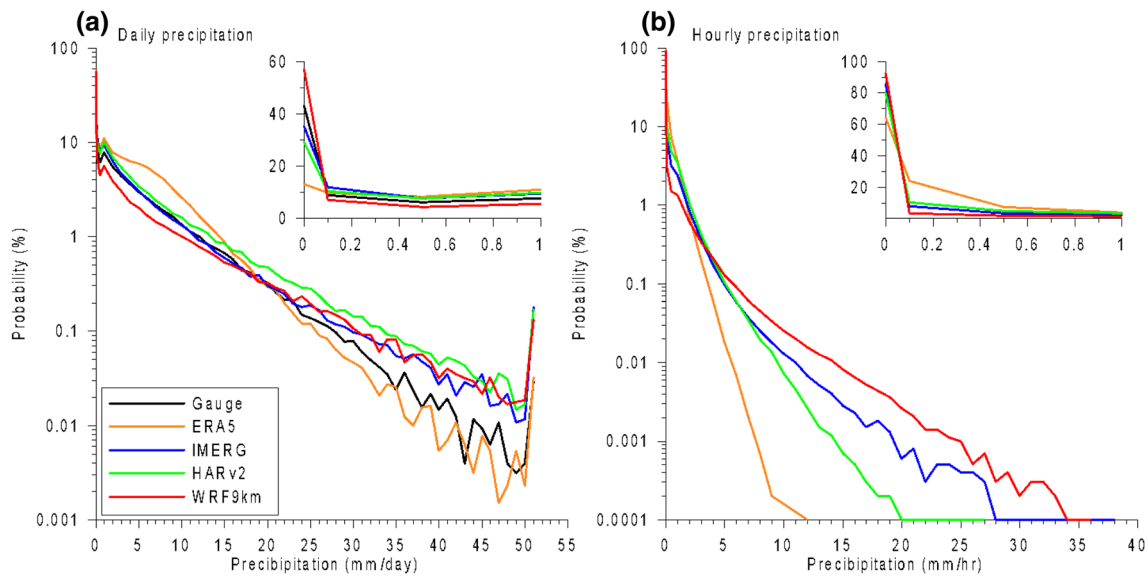


**Fig. 5** Probability density function (PDF) of **a** daily precipitation (mm/day) averaged over 83 gauges, ERA5, IMERG, HARv2, and WRF9km, **b** same as **(a)** but for hourly precipitation (mm/h; in situ observation is not shown)

lower frequency of hours with hourly precipitation larger than 4.0 mm than all the other data sets.

Overall, the observed summer mean precipitation over the whole TP was reproduced well by WRF9km. The IMERG precipitation agreed quite well with gauge observations, and this was further used as observed truth for evaluating simulated precipitation over the NWTP, where there are no available gauge stations (Fig. 1). The HARv2 precipitation was close to that of ERA5. This could be because of the daily re-initialization strategy utilized in HARv2 that cannot accurately address the possible mechanism behind the overestimation in ERA5 (e.g., Ma et al.

2021a). Hence, in what follows, we focus on the further evaluation of ERA5 and WRF9km.

### 3.2 Summer precipitation over the NWTP

Summer mean precipitation obtained from WRF9km was compared with that of ERA5 and IMERG to assess the ability of WRF9km to capture the climatological mean condition over the NWTP. As can be seen in Fig. 6, the latitudinal variation in the summer mean precipitation of IMERG was generally captured well by WRF9km, especially over the NWTP. A clear dry bias was found in WRF9km over the southern TP (south of 33° N), which will be discussed below.

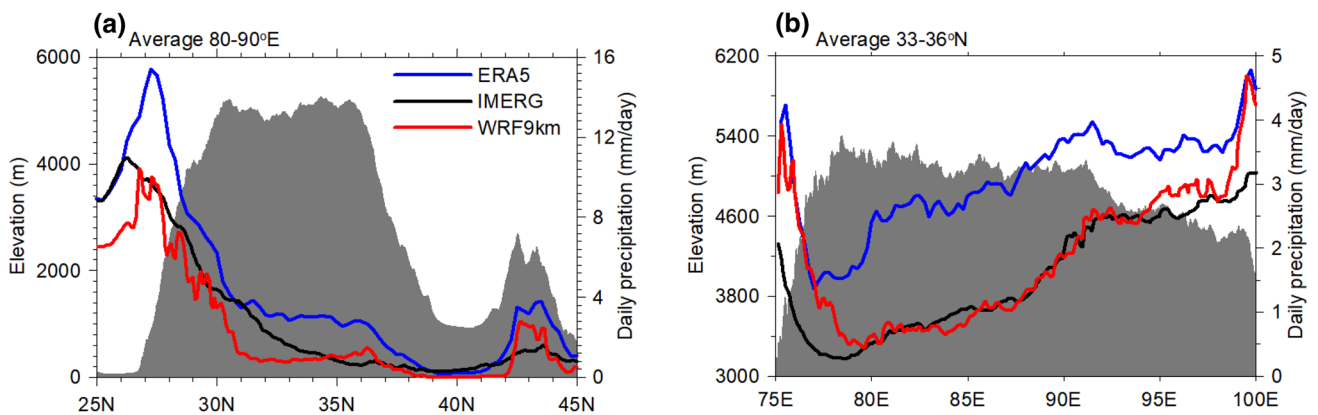


**Fig. 6** **a** Latitude evolution (averaged between 80° and 90° E) and **b** longitude evolution (averaged between 33° and 36° N) of summer (June–July–August) mean precipitation (mm/day) during 2000–2019

from ERA5, downscaling driven by ERA5 (WRF9km), and IMERG. The gray shaded area shows the mean elevation



Compared with WRF9km and IMERG, ERA5 overestimated summer precipitation, especially over the NWTP. Furthermore, the overestimated precipitation in ERA5 extended to the east of 95° E, while the longitudinal variation in IMERG precipitation was captured well by WRF9km (Fig. 6b). Over the western TP, between 75° and 80° E, precipitation from both WRF9km and ERA5 was higher than that of IMERG.

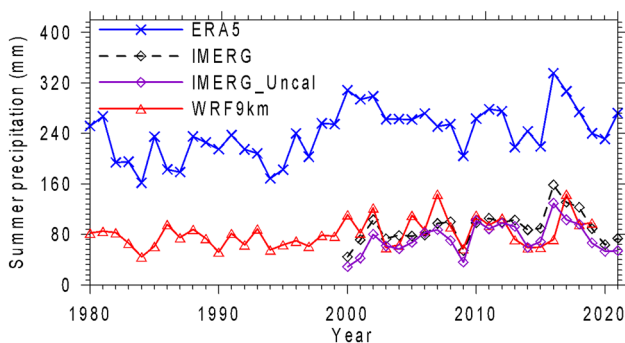


**Fig. 7** Time series of the interannual variation in summer total precipitation (mm) averaged over the region [33°–36° N, 80°–90° E] from ERA5, WRF9km, IMERG, and IMERG\_Uncal during the period 1980–2019

This appears to be reasonable because the underestimation of IMERG precipitation has previously been reported over this region (Li et al. 2020).

The annual variation in summer precipitation from WRF9km and ERA5 over the NWTP (33°–36° N, 80°–90° E) was further evaluated on based on the IMERG precipitation (Fig. 7). Compared with the IMERG precipitation, the summer precipitation over the region was vastly overestimated in ERA5, by 177% between 2000 and 2019. The overestimated precipitation in ERA5 was consistent over the study period. In contrast, WRF9km accurately reproduced the summer mean precipitation over the NWTP, with only a slight dry bias (–4%).

The overestimated precipitation in the study region in ERA5 could also be related to strong convection, which leads to a large contribution of convective precipitation to the total precipitation, and strong northward water vapor transportation. Over the NWTP, the mean contribution from convective precipitation to total summer precipitation was between 47% and 71% for ERA5 (figure not shown), which is far more than that of satellite-based products, with ratios of around 10% (Kukulies et al. 2020). The vertical distribution of the CCF from ERA5, WRF9km, and satellite

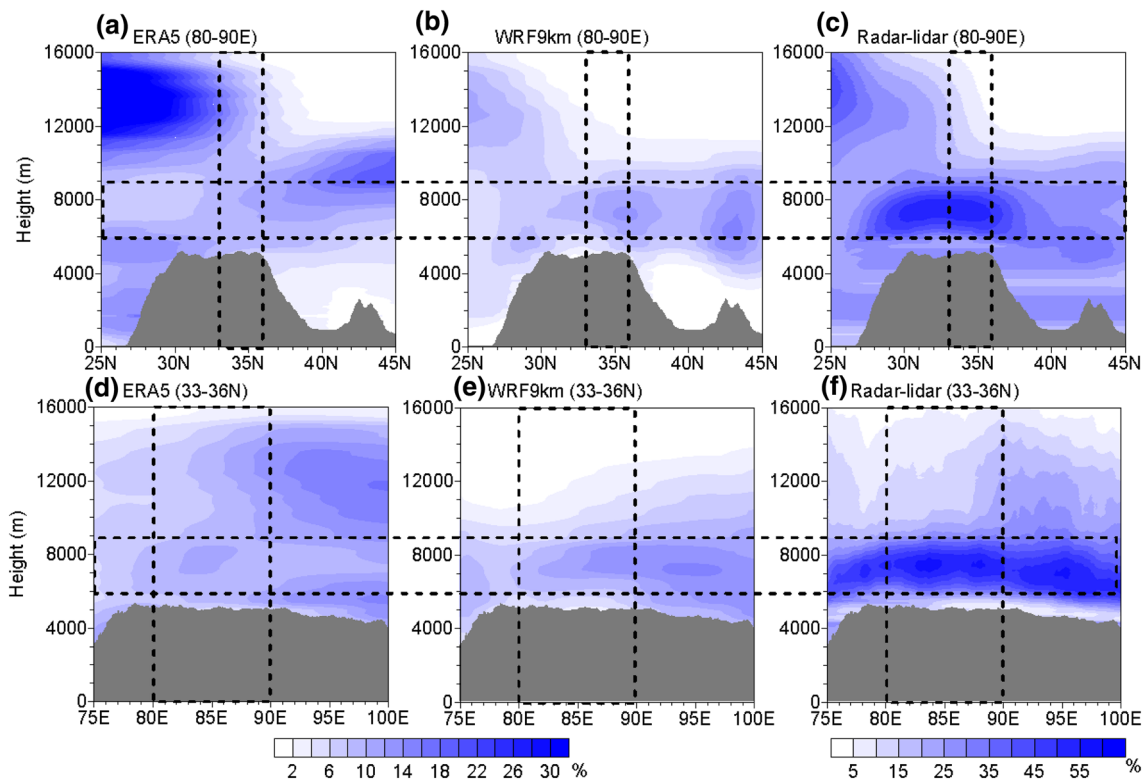


**Fig. 8** Vertical profile of cloud fraction (%) averaged during summer 2006–2010 between a–c 80°–90° E and d–f 33°–36° N from a, d ERA5, b, e WRF9km, and c, f satellite products (horizontal dashed lines enclose the center of cloud fraction over the plateau according

to satellite observations; vertical dashed lines in (a–c) enclose the region 33°–36° N, and those in (d–f) enclose the region 80°–90° E. The gray shaded area shows the mean elevation

observation was further compared (Fig. 8). In general, both ERA5 and WRF9km underestimated the CCF over the plateau compared with the satellite observation. Relatively speaking, the observed vertical location of the center of the CCF over the TP was reproduced better by WRF9km than by ERA5. This was especially true over the NWTP, where the observed center of the CCF was approximately 7 km above sea level. However, more clouds were found in ERA5 over the upper levels and to the north of the NWTP. This could be caused by the strong vertical motion and enhanced northward water vapor transportation in ERA5, inducing more (convective) precipitation over the study region; this will be further investigated below.

### 3.3 Summer mean circulation

To explore the mechanism behind the overestimated precipitation over the NWTP, summer mean pressure level circulation patterns (meridional and vertical winds; v-w) from ERA5 and WRF9km were examined (Fig. 9). Similar to the results of Feng and Zhou (2012), we found that in ERA5 in summer, a lower-level northward transport from the Indian summer monsoon meets a southward lower-level wind from the north of the TP between 33°–35° N, which induces a vertical motion over the region. In contrast, we found that in WRF9km, the two lower-level winds meet over the region south of 33° N, which is associated with a stronger northerly wind close to the surface over the study region. Compared with ERA5, WRF9km showed a weaker vertical motion over the NWTP, which supports the hypothesis that a higher fraction of upper-level cloud in ERA5 is associated with a strong vertical motion (Fig. 10). The strong vertical motion is connected to a stronger southerly wind at low levels in ERA5 than that in WRF9km, which is caused by the northward movement of the lower-level convergence zone. More specifically, compared with ERA5, WRF9km showed a weakened vertical motion between 33°–35° N and

lower amounts of precipitation. This indicates that the strong vertical motion in ERA5 very likely leads to more convective precipitation over the NWTP, which in turn leads to overestimated precipitation.

Lower-level wind at 500 hPa was also analyzed to examine the robustness of the above-mentioned results (Fig. 10). The climatological mean horizontal wind vector of WRF9km was fairly similar to ERA5 over the region outside the main body of the TP. However, large differences were found over the TP and downstream of the high mountains, indicating a large influence of topography on lower-level circulation. Compared with WRF9km, ERA5 showed a stronger southerly wind over the southern TP and weaker Westerlies effects; this is similar to the CPM simulations of Zhou et al. (2021). Further analysis showed that ERA5 overestimated the southerly wind over the southern TP, compared with the sounding observations. This indicates that ERA5 generates too strong a water vapor transport onto the plateau through the southern boundary, contributing to the overestimated precipitation over the NWTP. According to Lin et al. (2018) who have conducted several similar simulations over the TP using WRF model with resolutions of 30, 10, and 2 km, finer resolutions can improve resolving orographic drag over the complex terrain and other processes associated with heterogeneous surface forcing, reflected mostly in the weakened low-level wind speed. Thus, we deduce that better resolved orographic drag in WRF9km could be the main reason for reduced low-level southerly wind, as well as related water vapor transport. Besides the direct orographic drag, other processes associated with heterogeneous surface forcing such as glacier wind and mountain-valley circulation (Lin et al. 2018), which cannot be represented in ERA5 due to coarser resolution, can also affect the simulation of low-level wind fields.

In summary, stronger lower-level southerly wind and vertical motion over the NWTP were found in ERA5 compared with those of WRF9km. This leads to a northward

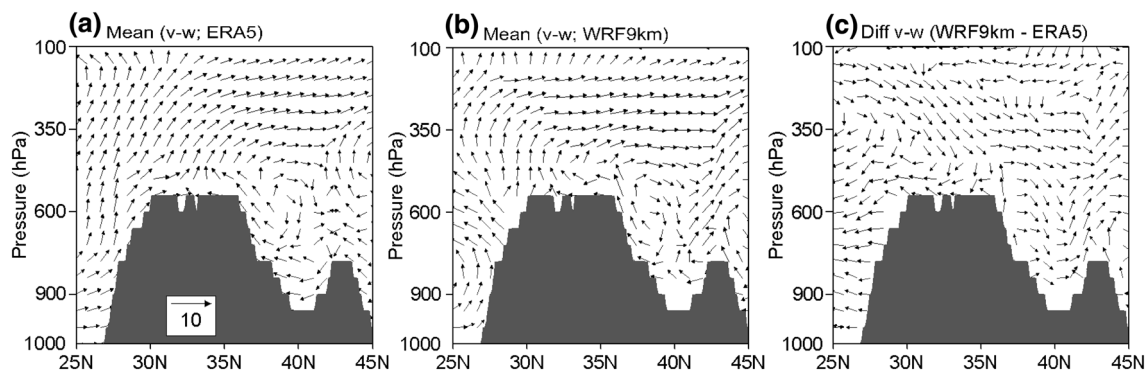
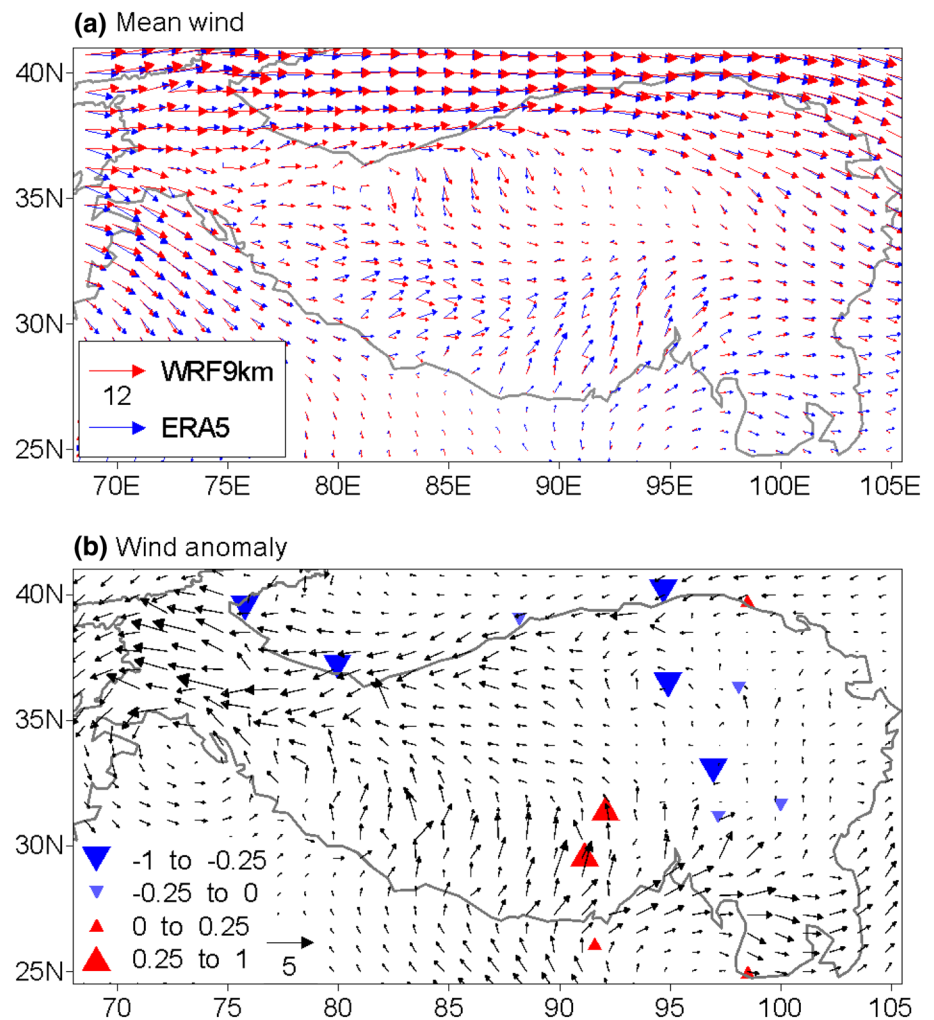


**Fig. 9** Latitude–pressure profile (averaged between 80° and 90° E) of the summer mean wind vector of meridional (v; m/s) and vertical (w;  $10^{-2}$  m/s) wind for **a** ERA5 and **b** WRF9km during the period 1980–

2019. The differences between WRF9km and ERA5 are shown in (c). The gray shaded area shows the mean elevation

**Fig. 10** **a** Spatial distribution of summer mean wind vector at 500 hPa averaged at 00:00 and 12:00 UTC during 1980–2019 from ERA5 (blue arrow) and WRF9km (red arrow). **b** Difference in wind vector between ERA5 and WRF9km (ERA5–WRF9km) at 500 hPa shown in **(a)** and the bias of meridional wind of ERA5 with reference to radiosonde observed meridional wind at 500 hPa (m/s) averaged at 00:00 and 12:00 during 1980–2019. The gray line represents the 2000 m contour



movement of the location where the southerly and northerly winds meet, where a vertical motion is triggered. The vertical motion is then enhanced, leading to more convective precipitation and further overestimation of summer precipitation over the NWTP.

#### 4 Conclusions and discussions

In this study, the summer precipitation over the NWTP in ERA5 and a WRF downscaling driven by ERA5 (i.e., WRF9km) have been evaluated against satellite-based precipitation (IMERG). The associated changes in the summer mean circulation patterns were also examined. Our results show that the summer precipitation over the NWTP is overestimated by ERA5, while such overestimations are substantially reduced by WRF9km. Further analysis shows that the overestimated precipitation in ERA5 is associated with a strong southerly wind over the southern TP and a weak northerly wind over the northern TP. This is connected to a northward movement of the location where the lower-level

southerly wind of the Indian summer monsoon and northerly wind branches of the Westerlies meet, which results in a northward movement of the lower-level convergence zone. The vertical motion is enhanced over the NWTP, which leads to more convective precipitation and consequently an overestimation of summer precipitation in ERA5 over the study region. Compared with ERA5, the southerly (northerly) wind over the southern (northern) TP is reduced (enhanced) by WRF9km, resulting in a more realistic simulation of the summer precipitation over the northern TP.

Overall, the WRF9km can accurately capture the summer mean precipitation over the TP, although a dry bias exists over the southern TP (south of 33° N). The dry bias could be caused by an unaccounted-for strong convective precipitation over the region (Kukulies et al. 2020), where there may be a high frequency of mesoscale convective systems in the summer season (Sugimoto and Ueno 2010) and convective systems over the region may occur in a more scattered manner and on small spatial scales (Kukulies et al. 2021). The dry bias over the southern TP may also be caused by an unaccounted-for channeling effect of valleys,

which can transport water vapor onto the high mountains through meridional canyons (Bookhagen and Burbank 2010). Convection-permitting model simulations with a horizontal resolution higher than 4 km may help to resolve this problem. For example, a CPM at 4 km has shown a better representation of mesoscale convective systems than one at 12 km (Prein et al. 2021), and CPM simulations at approximately 3.7 km by Zhou et al. (2021) and 2 km by Lin et al. (2018) have shown advantages in the simulation of water vapor transport onto the TP. The ability of RCMs to capture precipitation over the TP is expected to be further explored by the ongoing year-long and decadal simulations with a horizontal resolution of 4 km being conducted by the WCRP-CORDEX Flagship Pilot Study, Convection-Permitting Third Pole (CPTP; [http://rcg.gvc.gu.se/cordex\\_fps\\_cptp/](http://rcg.gvc.gu.se/cordex_fps_cptp/)).

Besides the impact of horizontal resolution on RCM simulations of precipitation over the TP, the domain size, especially the locations of boundaries, is another important influencing factor (Prein et al. 2022). The boundaries of the domain for a RCM should cover the major dynamic systems that affect the local circulation and precipitation. Taking the simulation of summer precipitation over the NWTP as an example, both the Westerlies and Asian summer monsoons, especially the Indian summer monsoon, and their interactions, have a large impact on the summer precipitation. Hence, the main parts of the two systems (25°–45° N) should be included in the domain setting. For example, as the domain was extended northwards to the north of 45° N, the precipitation over the NWTP was reduced in HARv2 compared with HAR (Wang et al. 2020). With the northern boundary located at approximately 45° N for the outer domain, the 500 hPa northerly wind over the northern TP was strengthened in WRF compared with ERA5 (Zhou et al. 2021), leading to an enhanced influence of the Westerlies on the local circulation and precipitation over the NWTP. A large domain may help reduce the influence of boundary forcing because RCMs can develop their own climatology with potentially modified large-scale climate structures (Giorgi 2019). This is especially important for high mountainous regions, such as the TP, where the enhanced topography exerts a considerable effect on atmospheric circulations, especially at lower levels. To validate this, we further explored the influence of domain size on the simulation of summer precipitation over the TP by comparing the WRF9km simulation with two case studies with different domains (Fig. S3). The model settings of the two case studies were similar to WRF9km except for the model domain, one with the northern boundary located at around 40° N and the other with a small domain covering the main body of the TP. The two experiments were conducted in the summer of 2014, with one month (May 2014) spin-up. Results showed that both experiments had higher summer precipitation over the NWTP compared to that of WRF9km (Fig. S4). Compared to WRF9km, both new experiments had a strong southerly

wind over the south of the central TP, while a weaker westerly wind over the north of the central TP, i.e., NWTP (Fig. S5). Therefore, these sensitivity experiments can be considered as a support to our speculation that a large domain may lead to better-captured low-level wind and summer precipitation over the NWTP.

Besides, to strengthen our knowledge of the driving mechanisms of summer precipitation over the TP, the influence of high mountains on the Westerlies and Asian summer monsoons and their interactions requires further investigation through high-resolution climate simulations and high-precision observational datasets, since the sparse gauge observation network and underestimated precipitation in observations caused by several factors, such as wind-caused undercatch and wetting and evaporation losses, could lead to some uncertainties in validating model simulations.

**Supplementary Information** The online version contains supplementary material available at <https://doi.org/10.1007/s00382-023-06672-3>.

**Acknowledgements** This work was supported by the Strategic Priority Research Program of the Chinese Academy of Sciences (Grant No. XDA20060401) and the Swedish Foundation for International Cooperation in Research and Higher Education (CH2019-8377). All the modeling experiments were funded by resources provided by the Swedish National Infrastructure for Computing (SNIC) at the National Supercomputer Centre in Sweden (NSC), partially funded by the Swedish Research Council through grant agreement no. 2018-0597. This is a contribution to the Swedish national strategic research program MERGE and no 8 to CORDEX-FPS-CPTP.

**Funding** Open access funding provided by University of Gothenburg. Strategic Priority Research Program of the Chinese Academy of Sciences, XDA20060401, Deliang Chen, Swedish Foundation for International Cooperation in Research and Higher Education, CH2019-8377, Tinghai Ou.

**Data availability** We thank the European Centre for Medium-Range Weather Forecasts (ECMWF) for providing the ERA5 reanalysis data (ERA5 data sets are available from <https://cds.climate.copernicus.eu/#/?search?text=ERA5&type=dataset>) and Dr. Xun Wang for help in retrieving the Asia Refined Analysis version 2 (HARv2) (HARv2 can be downloaded from [https://www.klima.tu-berlin.de/index.php?show=daten\\_har2&lan=en](https://www.klima.tu-berlin.de/index.php?show=daten_har2&lan=en)). The radiosonde observations from the Integrated Global Radiosonde Archive (IGRA) can be accessed through <https://www.noaa.gov/products/weather-balloon/integrated-global-radiosonde-archive>. The WRF9km simulations can be downloaded from the project site (<http://biggeo.gvc.gu.se/TPReanalysis/>) or by contacting the authors if the required data sets are not available online.

## Declarations

**Conflict of interest** The authors have not disclosed any conflict of interest.

**Open Access** This article is licensed under a Creative Commons Attribution 4.0 International License, which permits use, sharing, adaptation, distribution and reproduction in any medium or format, as long as you give appropriate credit to the original author(s) and the source, provide a link to the Creative Commons licence, and indicate if changes were made. The images or other third party material in this article are included in the article's Creative Commons licence, unless indicated

otherwise in a credit line to the material. If material is not included in the article's Creative Commons licence and your intended use is not permitted by statutory regulation or exceeds the permitted use, you will need to obtain permission directly from the copyright holder. To view a copy of this licence, visit <http://creativecommons.org/licenses/by/4.0/>.

## References

- An Z, Colman SM, Zhou W, Li X, Brown ET, Jull AJ et al (2012) Interplay between the Westerlies and Asian monsoon recorded in Lake Qinghai sediments since 32 ka. *Sci Rep* 2:619. <https://doi.org/10.1038/srep00619>
- Bookhagen B, Burbank DW (2010) Toward a complete Himalayan hydrological budget: spatiotemporal distribution of snowmelt and rainfall and their impact on river discharge. *J Geophys Res Earth Surf* 115:F03019. <https://doi.org/10.1029/2009JF001426>
- Bothe O, Fraedrich K, Zhu X (2011) Large-scale circulations and Tibetan Plateau summer drought and wetness in a high-resolution climate model. *Int J Climatol* 31:832–846. <https://doi.org/10.1002/joc.2124>
- Casella D, Panegrossi G, Sanò P, Marra AC, Dietrich S, Johnson BT, Kulie MS (2017) Evaluation of the GPM-DPR snowfall detection capability: comparison with CloudSat-CPR. *Atmos Res* 197:64–75. <https://doi.org/10.1016/j.atmosres.2017.06.018>
- Chen D, Dai A (2019) Precipitation characteristics in the community atmosphere model and their dependence on model physics and resolution. *J Adv Model Earth Syst* 11:2352–2374. <https://doi.org/10.1029/2018MS001536>
- Chen FH, Chen JH, Huang W (2009) A discussion on the westerly-dominated climate model in mid-latitude Asia during the modern interglacial period. *Earth Sci Front* 16:23–32 (in Chinese with English abstract)
- Chou MD, Suarez MJ (1999) A solar radiation parameterization for atmospheric studies. NASA Tech. Memo NASA/TM-1999-104606, p 40
- Curió J, Schiemann R, Hodges KI, Turner AG (2019) Climatology of Tibetan plateau vortices in reanalysis data and a high-resolution global climate model. *J Clim* 32(6):1933–1950. <https://doi.org/10.1175/JCLI-D-18-0021.1>
- Durre I, Vose RS, Wuertz DB (2006) Overview of the integrated global radiosonde archive. *J Clim* 19(1):53–68. <https://doi.org/10.1175/JCLI3594.1>
- Durre I, Yin X, Vose RS, Applequist S, Arnfield J (2018) Enhancing the data coverage in the integrated global radiosonde archive. *J Atmos Ocean Technol* 35(9):1753–1770. <https://doi.org/10.1175/JTECH-D-17-0223.1>
- Fassnacht SR (2004) Estimating alter-shielded gauge snowfall undercatch, snowpack sublimation, and blowing snow transport at six sites in the coterminous USA. *Hydrol Process* 18:3481–3492. <https://doi.org/10.1002/hyp.5806>
- Feng L, Zhou TJ (2012) Water vapor transport for summer precipitation over the Tibetan Plateau: multidata set analysis. *J Gerontol Ser A Biol Med Sci* 117:D20114. <https://doi.org/10.1029/2011JDO17012>
- Forsythe N, Fowler HJ, Li XF, Blenkinsop S, Pritchard D (2017) Karakoram temperature and glacial melt driven by regional atmospheric circulation variability. *Nature Clim Change* 7:664–670. <https://doi.org/10.1038/nclimate3361>
- Gao YH, Xu JW, Chen D (2015) Evaluation of WRF mesoscale climate simulations over the Tibetan Plateau during 1979–2011. *J Clim* 28(7):2823–2841. <https://doi.org/10.1175/JCLI-D-14-00300.1>
- Gao YH, Chen F, Jiang Y (2020a) Evaluation of a convection-permitting modeling of precipitation over the Tibetan Plateau and its influences on the simulation of snow-cover fraction. *J Hydrometeorol* 21:1531–1548. <https://doi.org/10.1175/JHM-D-19-0277.1>
- Gao YH, Chen F, Miguez-Macho G, Li X (2020b) Understanding precipitation recycling over the Tibetan Plateau using tracer analysis with WRF. *Clim Dyn* 55(9):2921–2937. <https://doi.org/10.1007/s00382-020-05426-9>
- Giorgi F (2019) Thirty years of regional climate modeling: where are we and where are we going next? *J Geophys Res Atmos* 124(11):5696–5723. <https://doi.org/10.1029/2018JD030094>
- Gómez B, Miguez-Macho G (2017) The impact of wave number selection and spin-up time in spectral nudging. *Q J Roy Meteor Soc* 143(705):1772–1786. <https://doi.org/10.1002/qj.3032>
- Gu H, Yu Z, Peltier WR, Wang X (2020) Sensitivity studies and comprehensive evaluation of RegCM4.6.1 high-resolution climate simulations over the Tibetan Plateau. *Clim Dyn* 54(7):3781–3801. <https://doi.org/10.1007/s00382-020-05205-6>
- Guo B, Zhou Y, Zhu J, Liu W, Wang F, Wang L et al (2016) Spatial patterns of ecosystem vulnerability changes during 2001–2011 in the three-river source region of the Qinghai-Tibetan Plateau, China. *J Arid Land* 8:23–35. <https://doi.org/10.1007/s40333-015-0055-7>
- Hersbach H, Bell B, Berrisford P, Hirahara S, Horányi A, Muñoz-Sabater J et al (2020) The ERA5 global reanalysis. *Q J Roy Meteor Soc* 146(730):1999–2049. <https://doi.org/10.1002/qj.3803>
- Hong SY, Noh Y, Dudhia J (2006) A new vertical diffusion package with an explicit treatment of entrainment processes. *Mon Weather Rev* 134(9):2318–2341. <https://doi.org/10.1175/MWR3199.1>
- Huffman GJ, Bolvin DT, Braithwaite D, Hsu K, Joyce R, Kidd C et al (2019a) NASA global precipitation measurement (GPM) integrated multi-satellite retrievals for GPM (IMERG) algorithm theoretical basis document (ATBD) version 06. NASA/GSFC, Greenbelt, MD, USA. [https://gpm.nasa.gov/sites/default/files/document\\_files/IMERG\\_ATBD\\_V06\\_0.pdf](https://gpm.nasa.gov/sites/default/files/document_files/IMERG_ATBD_V06_0.pdf). Accessed 15 Feb 2020
- Huffman GJ, Stocker EF, Bolvin DT, Nelkin EJ, Tan J (2019b) GPM IMERG final precipitation L3 half hourly 0.1 degree x 0.1 degree V06. Greenbelt, MD, Goddard Earth Sciences Data and Information Services Center (GES DISC). <https://doi.org/10.5067/GPM/IMERG/3B-HH/06>. Accessed 15 Feb 2020
- Iacono MJ, Delamere JS, Mlawer EJ, Shephard MW, Clough SA, Collins WD (2008) Radiative forcing by long-lived greenhouse gases: calculations with the AER radiative transfer models. *J Gerontol Ser A Biol Med Sci* 113:D13103. <https://doi.org/10.1029/2008JD009944>
- Jiménez PA, Dudhia J, González-Rouco JF, Navarro J, Montávez JP, García-Bustamante E (2012) A revised scheme for the WRF surface layer formulation. *Mon Weather Rev* 140(3):898–918. <https://doi.org/10.1175/MWR-D-11-00056.1>
- Kida H, Koide T, Sasaki H, Chiba M (1991) A new approach for coupling a limited area model to a GCM for regional climate simulations. *J Meteorol Soc Jpn Ser II* 69(6):723–728. [https://doi.org/10.2151/jmsj1965.69.6\\_723](https://doi.org/10.2151/jmsj1965.69.6_723)
- Kong W, Chiang J (2020) Interaction of the westerlies with the Tibetan Plateau in determining the Mei-Yu termination. *J Clim* 33(1):339–363. <https://doi.org/10.1175/JCLI-D-19-0319.1>
- Krishnan R, Shrestha AB, Ren G, Rajbhandari R, Saeed S, Sanjay J et al (2019) Unravelling climate change in the Hindu Kush Himalaya: rapid warming in the mountains and increasing extremes. In: Wester P, Mishra A, Mukherji A, Shrestha A (eds) *The Hindu Kush Himalaya assessment*. Springer, Cham, pp 57–97
- Kukulies J, Chen D, Wang H (2019) Temporal and spatial variations of convection and precipitation over the Tibetan Plateau based on recent satellite observations. Part I: cloud climatology derived from CloudSat and CALIPSO. *Int J Climatol* 39(14):5396–5412. <https://doi.org/10.1002/joc.6162>
- Kukulies J, Chen D, Wang M (2020) Temporal and spatial variations of convection, clouds and precipitation over the Tibetan Plateau

- from recent satellite observations. Part II: precipitation climatology derived from global precipitation measurement mission. *Int J Climatol* 40(11):4858–4875. <https://doi.org/10.1002/joc.6493>
- Kukulies J, Chen D, Curio J (2021) The role of mesoscale convective systems in precipitation in the Tibetan Plateau region. *J Geophys Res Atmos*. <https://doi.org/10.1029/2021JD035279>
- Lai HW, Chen HW, Kukulies J, Ou T, Chen D (2021) Regionalization of seasonal precipitation over the Tibetan Plateau and associated large-scale atmospheric systems. *J Clim* 34(7):2635–2651. <https://doi.org/10.1175/JCLI-D-20-0521.1>
- Latif A, Ilyas S, Zhang Y, Xin Y, Zhou L, Zhou Q (2019) Review on global change status and its impacts on the Tibetan Plateau environment. *J Plant Ecol* 12:917–930. <https://doi.org/10.1093/jpe/rtz038>
- Li BV, Pimm SL (2020) How China expanded its protected areas to conserve biodiversity. *Curr Biol* 30(22):R1334–R1340. <https://doi.org/10.1016/j.cub.2020.09.025>
- Li H, Song W (2021) Spatiotemporal distribution and influencing factors of ecosystem vulnerability on Qinghai-Tibet Plateau. *Int J Environ Res Public Health* 18:6508. <https://doi.org/10.3390/ijerph18126508>
- Li J, Yu R, Yuan W, Chen H, Sun W, Zhang Y (2015) Precipitation over East Asia simulated by NCAR CAM5 at different horizontal resolutions. *J Adv Model Earth Syst* 7(2):774–790. <https://doi.org/10.1002/2014MS000414>
- Li D, Yang K, Tang W, Li X, Zhou X, Guo D (2020) Characterizing precipitation in high altitudes of the western Tibetan plateau with a focus on major glacier areas. *Int J Climatol* 40(12):5114–5127. <https://doi.org/10.1002/joc.6509>
- Li P, Furtado K, Zhou T, Chen H, Li J (2021) Convection-permitting modelling improves simulated precipitation over the central and eastern Tibetan Plateau. *Q J Roy Meteor Soc* 147(734):341–362. <https://doi.org/10.1002/qj.3921>
- Li DH, Qi YC, Chen D (2022) Changes in rain and snow over the Tibetan Plateau based on IMERG and Ground-based observation. *J Hydrol* 606:127400. <https://doi.org/10.1016/j.jhydrol.2021.127400>
- Liang Y, Yang B, Wang M, Tang J, Sakaguchi K, Leung LR, Xu X (2021) Multiscale simulation of precipitation over East Asia by variable resolution CAM-MPAS. *J Adv Model Earth Syst*. <https://doi.org/10.1029/2021MS002656>
- Lim KSS, Hong SY (2010) Development of an effective double-moment cloud microphysics scheme with prognostic cloud condensation nuclei (CCN) for weather and climate models. *Mon Weather Rev* 138(5):1587–1612. <https://doi.org/10.1175/2009MWR2968.1>
- Lin C, Chen D, Yang K, Ou T (2018) Impact of model resolution on simulating the water vapor transport through the central Himalayas: implication for models' wet bias over the Tibetan Plateau. *Clim Dyn* 51(9):3195–3207. <https://doi.org/10.1007/s00382-018-4074-x>
- Lin Z, Guo W, Jia L, Yao X, Zhou Z (2020) Climatology of Tibetan Plateau vortices derived from multiple reanalysis datasets. *Clim Dyn* 55(7):2237–2252. <https://doi.org/10.1007/s00382-020-05380-6>
- Liu X, Yin ZY (2001) Spatial and temporal variation of summer precipitation over the Eastern Tibetan Plateau and the North Atlantic Oscillation. *J Clim* 14:2896–2909
- Liu C, Ikeda K, Rasmussen R, Barlage M, Newman AJ, Prein AF et al (2017) Continental-scale convection-permitting modeling of the current and future climate of North America. *Clim Dyn* 49(1):71–95. <https://doi.org/10.1007/s00382-016-3327-9>
- Ma Y, Zhang Y, Yang D, Farhan SB (2015) Precipitation bias variability versus various gauges under different climatic conditions over the Third Pole Environment (TPE) region. *Int J Climatol* 35:1201–1211. <https://doi.org/10.1002/joc.4045>
- Ma M, Hui P, Liu D, Zhou P, Tang J (2021a) Convection-permitting regional climate simulations over Tibetan Plateau: re-initialization versus spectral nudging. *Clim Dyn* 58:1719–1735. <https://doi.org/10.1007/s00382-021-05988-2>
- Ma Q, Li Y, Feng H, Yu Q, Zou Y, Liu F, Pulatov B (2021b) Performance evaluation and correction of precipitation data using the 20-year IMERG and TMPA precipitation products in diverse subregions of China. *Atmos Res* 249:105304. <https://doi.org/10.1016/j.atmosres.2020.105304>
- Mace GG, Zhang Q (2014) The CloudSat radar-lidar geometrical profile product (RL-GeoProf): Updates, improvements, and selected results. *J Geophys Res Atmos* 119(15):9441–9462. <https://doi.org/10.1002/2013JD021374>
- Mai X, Qiu X, Yang Y, Ma Y (2020) Impacts of spectral nudging parameters on dynamical downscaling in summer over mainland China. *Front Earth Sci*. <https://doi.org/10.3389/feart.2020.574754>
- Marchand R, Mace GG, Ackerman T, Stephens G (2008) Hydrometeor detection using Cloudsat—an earth-orbiting 94-GHz cloud radar. *J Atmos Ocean Technol* 25(4):519–533. <https://doi.org/10.1175/2007JTECHA1006.1>
- Molnar P, Boos WR, Battisti DS (2010) Orographic controls on climate and paleo-climate of Asia: thermal and mechanical roles for the Tibetan Plateau. *Annu Rev Earth Planet Sci* 38:77–102. <https://doi.org/10.1146/annurev-earth-040809-152456>
- Ou T, Chen D, Chen X, Lin C, Yang K, Lai HW, Zhang F (2020) Simulation of summer precipitation diurnal cycles over the Tibetan Plateau at the gray-zone grid spacing for cumulus parameterization. *Clim Dyn* 54:3525–3539. <https://doi.org/10.1007/s00382-020-05181-x>
- Prein AF, Rasmussen RM, Wang D, Giangrande SE (2021) Sensitivity of organized convective storms to model grid spacing in current and future climates. *Philos Trans R Soc Math Phys Eng Sci* 379(2195):20190546. <https://doi.org/10.1098/rsta.2019.0546>
- Prein AF, Ban N, Ou T, Tang JP, Sakaguchi K, Collier E et al (2022) Towards ensemble-based kilometer-scale climate simulations over the third pole region. *Clim Dyn*. <https://doi.org/10.1007/s00382-022-06543-3>
- Reuter HI, Nelson A, Jarvis A (2007) An evaluation of void-filling interpolation methods for SRTM data. *Int J Geogr Inf Sci* 21(9):983–1008. <https://doi.org/10.1080/13658810601169899>
- Schiemann R, Lüthi D, Schär C (2009) Seasonality and interannual variability of the westerly jet in the Tibetan Plateau region. *J Clim* 22:2940–2957. <https://doi.org/10.1175/2008JCLI2625.1>
- Shen M, Wang S, Jiang N, Sun J, Cao R, Ling X et al (2022) Plant phenology changes and drivers on the Qinghai-Tibetan Plateau. *Nat Rev Earth Environ* 3:633–651. <https://doi.org/10.1038/s43017-022-00317-5>
- Skamarock WC, Klemp JB, Dudhia J, Gill DO, Barker D, Duda MG et al (2008) A description of the advanced research WRF version 3 (no. NCAR/TN-475+STR). University Corporation for Atmospheric Research. <https://doi.org/10.5065/D68S4MVH>
- Su B, Xiao C, Chen D, Huang Y, Che Y, Zhao H et al (2022) Glacier change in China over past decades: spatiotemporal patterns and influencing factors. *Earth-Sci Rev* 226:103926. <https://doi.org/10.1016/j.earscirev.2022.103926>
- Sugimoto S, Ueno K (2010) Formation of mesoscale convective systems over the eastern Tibetan Plateau affected by plateau-scale heating contrasts. *J Geophys Res Atmos* 115:D16105. <https://doi.org/10.1029/2009JD013609>
- Sun J, Yang K, Guo W, Wang Y, He J, Lu H (2020) Why has the inner Tibetan Plateau become wetter since the mid-1990s? *J Climate* 33(19):8507–8522. <https://doi.org/10.1175/JCLI-D-19-0471.1>
- Sun H, Su F, Yao T, He Z, Tang G, Huang J et al (2021) General overestimation of ERA5 precipitation in flow simulations for High Mountain Asia basins. *Environ Res Commun* 3(12):121003. <https://doi.org/10.1088/2515-7620/ac40f0>

- Tang G, Clark MP, Papalexiou SM, Ma Z, Hong Y (2020) Have satellite precipitation products improved over last two decades? A comprehensive comparison of GPM IMERG with nine satellite and reanalysis datasets. *Remote Sens Environ* 240:111697. <https://doi.org/10.1016/j.rse.2020.111697>
- Tewari M, Chen F, Wang W, Dudhia J, LeMone MA, Mitchell K et al (2004) Implementation and verification of the unified NOAA land surface model in the WRF model 20th conference on weather analysis and forecasting/16th conference on numerical weather prediction, 11–15. American Meteorological Society, Seattle, WA, US
- Tong K, Su F, Yang D, Zhang L, Hao Z (2014) Tibetan Plateau precipitation as depicted by gauge observations, reanalyses and satellite retrievals. *Int J Climatol* 34(2):265–285. <https://doi.org/10.1002/joc.3682>
- von Storch H, Langenberg H, Feser F (2000) A spectral nudging technique for dynamical downscaling purposes. *Mon Weather Rev* 128(10):3664–3673. [https://doi.org/10.1175/1520-0493\(2000\)128%3c3664:ASNTFD%3e2.0.CO;2](https://doi.org/10.1175/1520-0493(2000)128%3c3664:ASNTFD%3e2.0.CO;2)
- Wan G, Yang M, Liu Z, Wang X, Liang X (2017) The precipitation variations in the Qinghai-Xizang (Tibetan) Plateau during 1961–2015. *Atmosphere* 8:80. <https://doi.org/10.3390/atmos8050080>
- Wang X, Pang G, Yang M, Zhao G (2017) Evaluation of climate on the Tibetan Plateau using ERA-Interim reanalysis and gridded observations during the period 1979–2012. *Quatern Inter* 444:76–86. <https://doi.org/10.1016/j.quaint.2016.12.041>
- Wang X, Pang G, Yang M (2018) Precipitation over the Tibetan Plateau during recent decades: a review based on observations and simulations. *Int J Climatol* 38(3):1116–1131. <https://doi.org/10.1002/joc.5246>
- Wang X, Tolksdorf V, Otto M, Scherer D (2020) WRF-based dynamical downscaling of ERA5 reanalysis data for High Mountain Asia: towards a new version of the High Asia Refined analysis. *Int J Climatol* 41(1):743–762. <https://doi.org/10.1002/joc.6686>
- Wang X, Chen D, Pang G, Anwar SA, Ou T, Yang M (2021) Effects of cumulus parameterization and land-surface hydrology schemes on Tibetan Plateau climate simulation during the wet season: insights from the RegCM4 model. *Clim Dyn* 57(7):1853–1879. <https://doi.org/10.1007/s00382-021-05781-1>
- Weltzin JF, Loik ME, Schwinning S, Williams DG, Fay PA, Haddad BM et al (2003) Assessing the response of terrestrial ecosystems to potential changes in precipitation. *Bioscience* 53:941–952. [https://doi.org/10.1641/0006-3568\(2003\)053\[0941:ATROTE\]2.0.CO;2](https://doi.org/10.1641/0006-3568(2003)053[0941:ATROTE]2.0.CO;2)
- Wu GX, Duan AM, Liu YM, Mao JY, Ren RC, Bao Q et al (2015) Tibetan Plateau climate dynamics: recent research progress and outlook. *National Sci Rev* 2:100–116. <https://doi.org/10.1093/nsr/nwu045>
- Xiong J, Yong Z, Wang Z, Cheng W, Li Y, Zhang H, Ye C, Yang Y (2019) Spatial and temporal patterns of the extreme precipitation across the Tibetan Plateau (1986–2015). *Water* 11:1453. <https://doi.org/10.3390/w11071453>
- Xu X, Lu C, Shi X, Gao S (2008) World water tower: an atmospheric perspective. *Geophys Res Lett* 35:L20815. <https://doi.org/10.1029/2008GL035867>
- Yang D, Kane DL, Hinzman LD, Goodison BE, Metcalfe JR, Louie PYT et al (2000) An evaluation of the Wyoming Gauge system for snowfall measurement. *Water Resour Res* 36:2665–2677. <https://doi.org/10.1029/2000WR900158>
- Yang M, Wang X, Pang G, Wan G, Liu Z (2019) The Tibetan Plateau cryosphere: observations and model simulations for current status and recent changes. *Earth Sci Rev* 190:353–369. <https://doi.org/10.1016/j.earscirev.2018.12.018>
- Yao T, Thompson L, Yang W, Gao Y, Guo X et al (2012) Different glacier status with atmospheric circulations in Tibetan Plateau and surroundings. *Nat Clim Change* 2(9):663–667. <https://doi.org/10.1038/nclimate1580>
- Yao T, Masson-Delmotte V, Gao J, Yu W, Yang X, Risi C et al (2013) A review of climatic controls on  $\delta^{18}O$  in precipitation over the Tibetan Plateau: observations and simulations. *Rev Geophys* 51:525–548. <https://doi.org/10.1002/rog.20023>
- Ye D (1981) Some characteristics of the summer circulation over the Qinghai-Xizang (Tibet) Plateau and its neighborhood. *Bull Am Meteorol Soc* 62(1):14–19. [https://doi.org/10.1175/1520-0477\(1981\)062%3c0014:SCOTSC%3e2.0.CO;2](https://doi.org/10.1175/1520-0477(1981)062%3c0014:SCOTSC%3e2.0.CO;2)
- You Q, Chen D, Wu F, Pepin N, Cai Z, Ahrens B et al (2020) Elevation dependent warming over the Tibetan Plateau: patterns, mechanisms and perspectives. *Earth Sci Rev* 210:103349. <https://doi.org/10.1016/j.earscirev.2020.103349>
- Yu X, Zhang L, Zhou T, Liu J (2021) The Asian subtropical westerly jet stream in CRA-40, ERA5, and CFSR reanalysis data: comparative assessment. *J Meteorol Res* 35(1):46–63. <https://doi.org/10.1007/s13351-021-0107-1>
- Zhang Y, Ren Y, Ren G, Wang G (2019a) Bias correction of gauge data and its effect on precipitation climatology over mainland China. *J Appl Meteorol Climatol* 58:2177–2196. <https://doi.org/10.1175/JAMC-D-19-0049.1>
- Zhang C, Tang Q, Chen D, van der Ent RJ, Liu X, Li W, Haile GG (2019b) Moisture source changes contributed to different precipitation changes over the northern and southern Tibetan Plateau. *J Hydrometeorol* 20(2):217–229. <https://doi.org/10.1175/JHM-D-18-0094.1>
- Zhou X, Yang K, Ouyang L, Wang Y, Jiang Y, Li X, Chen D, Prein A (2021) Added value of kilometer-scale modeling over the third pole region: a CORDEX-CPTP pilot study. *Clim Dyn* 57(7):1673–1687. <https://doi.org/10.1007/s00382-021-05653-8>
- Zhu L, Lü X, Wang J, Peng P, Kasper T, Daut G et al (2015) Climate change on the Tibetan Plateau in response to shifting atmospheric circulation since the LGM. *Sci Rep* 5:13318. <https://doi.org/10.1038/srep13318>
- Zou D, Zhao L, Sheng Y, Chen J, Hu G, Wu T et al (2017) A new map of permafrost distribution on the Tibetan Plateau. *Cryosphere* 11(6):2527–2542. <https://doi.org/10.5194/tc-11-2527-2017>

**Publisher's Note** Springer Nature remains neutral with regard to jurisdictional claims in published maps and institutional affiliations.